Pre-Launch Calibration of the HYPSO-1 Cubesat Hyperspectral Imager

Marie Bøe Henriksen, Elizabeth Frances Prentice, and Tor Arne Johansen
Department of Engineering Cybernetics, Center for Autonomous Marine Operations and Systems
Norwegian University of Science and Technology
7034 Trondheim, Norway

Fred Sigernes
Department of Arctic Geophysics
University Center in Svalbard
N-9171, Longyearbyen, Norway

Abstract— **This paper describes the pre-launch optical calibration and characterization of the hyperspectral imager for the HYPerspectral Smallsat for ocean Observation (HYPSO-1) cubesat. The aim of the mission is to observe algal blooms and other ocean color phenomena from a cubesat platform using a pushbroom HyperSpectral Imager (HSI) design based on Commercial Off-The-Shelf (COTS) components. A thorough pre-launch characterization is necessary to study the expected quality of the hyperspectral data, and to identify any potential deficiencies and weaknesses in the design. The calibration work was focused on spectral and radiometric calibration, characterizing smile and keystone, and measuring the polarization sensitivity. Smile and keystone effects were noticeable during preliminary tests, and were therefore characterized to provide necessary corrections. From spectral calibration data the average bandwidth was found to be 3.93 nm, which is close to the theoretical value of 3.3 nm. The full spectral range of the instrument was found to be 224 to 962 nm. The radiometric calibration data was also used to characterize the sensor performance, which was shown to be as expected. Smile was measured to be 3.58 pixels and 0.38 pixels before and after correction, respectively, while keystone was found to be 1.72 pixels before correction and 0.56 pixels after correction. The polarization sensitivity was within the required value of 5% for wavelengths above 410 nm. Finally, a spatial focus test was performed indicating best spatial focus at the center wavelength of 600 nm. Future work for the HYPSO-1 mission includes developing methods for in-orbit calibration, and for future HYPSO missions a more thorough characterization and correction for varying temperature is suggested.**

TABLE OF CONTENTS

1. INTRODUCTION

The use of HyperSpectral Imagers (HSIs) is increasing in many fields, remote sensing among them. As the technology develops and matures, components are getting both smaller and cheaper, and designs are continuously being presented making it possible for research groups and commercial companies to build and use these instruments. Recent progress makes compact designs viable [1], [2], which can further be combined with drones and small satellite platforms such as cubesats.

This has lead to development of the HYPerspectral Smallsat for ocean Observations (HYPSO) mission at the Norwegian University of Science and Technology (NTNU), a cubesat mission with the goal of observing algal blooms and other ocean color phenomena using a pushbroom HSIs based on Commercial Off-The-Shelf (COTS) components [3], [4]. The 6U cubesat will fly at a 500 km altitude sun-synchronous orbit and perform a slew maneuver to scan a target area capturing overlapping frames to increase spatial resolution and Signal-to-Noise Ratio (SNR), as described in Grøtte et al. [3].

Prior to launch, laboratory calibration and characterization of the instrument is important to ensure proper data quality, and to identify any potential issues in the final assembled configuration. A list of about thirty characteristics suggested for HSI specification is presented in Skauli et al.[5]. However, a large calibration campaign can be both time consuming and expensive to perform. In Bowles et al. [6], it is suggested that the calibration cost should be consistent with the cost and need of the instrument and its application. As the HYPSO-1 HSI is a small instrument built with COTS components in a university environment, a smaller calibration campaign focused on verifying a set of the HYPSO-1 payload requirements was planned. As the laboratory facilities, equipment and time were limited, known issues such as smile and keystone characterization were prioritized over, for example, characterizing the Point Spread Function (PSF) or doing detailed stray light characterization.

This paper describes the instruments, equipment and methods used for the pre-launch calibration campaign of the HYPSO-1 hyperspectral imager. The results are presented and discussed, and finally compared to the relevant instrument requirements set by the mission.

978-1-6654-3760-8/22/$31.00

2. INSTRUMENT

The HYPSO-1 main payload is a pushbroom HSI with a transmitting grating as the dispersive element. It is built using COTS components, based on the design presented in Henriksen et al. [7]. Some adjustments were made to the components to prepare them for the space environment, as described in Prentice et al. [4]. Among these were modifying the COTS objectives by fixing the aperture and focus, cleaning the objectives to remove grease, machining a detector housing in aluminum to avoid plastic parts, machining a custom designed slit tube to minimize the number of parts needed, and designing a custom platform to fix the optical train and ensure no parts were able to move during anticipated shock and vibrations at launch.

A summary of the main specifications of the HSI can be seen in Table 1. The spectral range required for the mission is 400 nm to 800 nm, but a larger spectral range reaches the full sensor. A part of the calibration is therefore to ensure that the desired range is within the selected Area Of Interest (AOI) used operationally in the mission. This smaller AOI was chosen to reduce data for faster downlinking in orbit. In theory the full spectral range reaching the sensor could be used, but it is limited by an anti-reflection coating on the lenses that blocks light below 400 nm, low Quantum Efficiency (QE) of the CMOS sensor, and second order diffraction effects that appear above 800 nm. The pre-launch calibration and characterization therefore focuses on this spectral range. It is possible to expand the desired spectral range to include 800 nm to 900 nm by increasing the AOI. This can be useful if attempting to characterize and remove second order light with in-flight data as performed in Li et al. [8]. Corrected longer wavelengths (above 700 nm) can then, for example, be used for atmospheric correction [9].

Table 1: **Specifications of the hyperspectral imager.**

Parameter	Specification
Sensor	Sony IMX249
Image size	(1936, 1216) pixels
Area of interest[1]	pixel (428:1508, 266:950)
Bit depth	12-bit
Spectral range	400 - 800 nm
Grating	300 grooves/mm, transmission
Slit dimensions	7 mm x 50 μm
Theoretical FWHM	3.33 nm

[1] Pre-selected AOI, can be changed if needed.

The theoretical bandwidth, the Full Width at Half Maximum (FWHM), is calculated as

$$\text{FWHM} = \frac{wa\cos(\alpha)}{kf} = 3.33 \text{ nm}, \quad (1)$$

where $w = 50$ μm is the slit width, $a = 3.33$ μm is the grating groove spacing, $\alpha = 0^\circ$ is the incident angle of the incoming light, $k = 1$ is the first spectral order, and $f = 50$ mm is the focal length of the middle objective that collimates the light onto the grating.

An image of the HYPSO-1 optical payload containing both the HSI and a standard Red-Green-Blue (RGB) color camera is shown in Figure 1. The RGB camera is used for geospatial validation of the hyperspectral images. They are both mounted on the same platform to fix their orientation relative to each other, which in the image is fastened onto a mounting plate. The plate is used for testing, and is not a part of the flight model payload. In addition to the HSI and RGB, the payload includes an electronics stack used for interface and control with the rest of the satellite, not shown in the image.

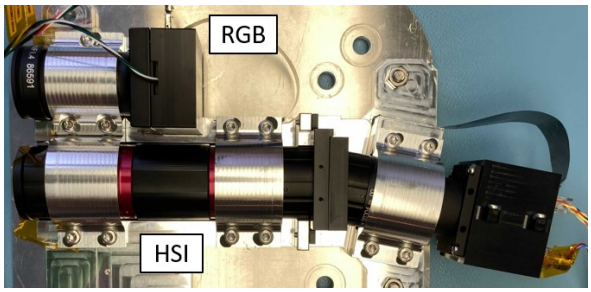

Figure 1: The optical payload unit of the HYPSO-1 cubesat, consisting of a small RGB camera (top of image) and the hyperspectral imager (bottom of image).

A selection of the HSI requirements for the HYPSO-1 mission are shown in Table 2. The requirements shown are the ones that have been addressed in this calibration campaign.

Table 2: **Set of hyperspectral imager requirements.**

Parameter	Requirement
Sensor response	Linear
FWHM	< 5 nm
Smile after correction	< 1 pixel
Keystone after correction	< 1 pixel
Polarization sensitivity	$< 5\%$
Uncertainty of polarization sensitivity	$< 0.2\%$

Three optically identical models of the hyperspectral imager were made, one Engineering Model (EM), one Qualification Model (QM) and one Flight Model (FM), where the FM will be the one launched on the cubesat. The EM and QM were used for development and testing to minimize stress on the FM. For the polarization sensitivity test the EM was used, but the results are expected to hold for the FM since the polarization sensitivity should not change between the models. The data from the calibration campaign includes data for the calibrations, investigation of sensor characteristics, FWHM, smile and keystone correction and the spatial focus test, which were all completed with the FM prior to launch.

3. CALIBRATION

This section describes the spectral and radiometric calibration of the HSI. The data from spectral calibration was further used to measure the FWHM in Section 5, while the radiometric calibration data was also used to assess the sensor response described in Section 4. The main equipment used was an integrating sphere and two spectral calibration lamps. The integrating sphere was a 30 cm radius (Model ISS-30VA, Gigahertz Optik) with a 10 cm output port and certified tungsten halogen lamp with reference radiance from 400 nm to 2500 nm with a 10 nm resolution. The spectral calibration lamps were argon (Newport model 6030) and mercury-argon (Newport model 6035) with emission lines in the 400 to 800 nm range.

Spectral calibration

For spectral calibration the argon and mercury-argon spectral lamps were used in combination with the integrating sphere. The spectral lamps were mounted in a small input port of the sphere to ensure even illumination. The HSI was placed in front of the sphere outlet and 10 images were taken for each lamp with an exposure time that let the strongest peak in the image approach saturation. A combined image, with both the argon and the mercury-argon lines, is shown in Figure 2.

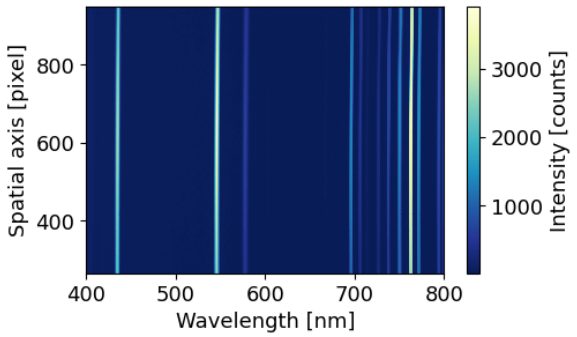

Figure 2: Spectral calibration frame, with both the argon and mercury-argon emission lines.

For the wavelength-pixel relation, or spectral calibration, different order polynomials were fit to the data. The spectral pixel position of each peak was detected and compared to the known positions of the peaks to estimate the polynomial coefficients. The Root Mean Square Error (RMSE) was calculated for each polynomial to determine the fit, as shown in Table 3. The third order polynomial was chosen to describe the wavelength-pixel relation since it minimized the RMSE without increasing complexity.

Table 3: **RMSE of polynomial fits of different orders.**

Order	RMSE
1	0.98
2	0.16
3	0.10
4	0.08

The third order polynomial fit is described by

$$\lambda \approx a_0 + a_1 \cdot p + a_2 \cdot p^2 + a_3 \cdot p^3, \tag{2}$$

where λ is the wavelength, p is the spectral pixel index and a_0, a_1, a_2 and a_3 are the spectral calibration coefficients. The calculated values of the coefficients are shown in Table 4.

Table 4: **Spectral calibration coefficients.**

Coefficient	Value
a_0	2.24e+02
a_1	3.84e-01
a_2	4.75e-06
a_3	-3.21e-09

From the spectral calibration coefficients the full spectral range on the image sensor is found to be 224 to 962 nm. The chosen wavelength range of 400 to 800 nm is located between spectral pixel 456 and 1502 on the sensor.

Radiometric calibration

Radiometric calibration data was collected using the integrating sphere where the HSI was placed in front of the sphere outlet. The HSI was set at 25 ms exposure time and 10 images were captured. A set of dark images were also taken using the same exposure time, but with the lens cap on the camera and all light sources in the room turned off. The dark images were used to estimate the average background signal in the images, which is described in Section 4.

The normalized signal in a frame, S [counts/sec], was estimated by averaging the 10 captured frames to reduce random fluctuations, removing the estimated background signal, and scaling the image by the exposure time. The radiometric calibration coefficient K was then calculated as

$$K = \frac{L}{S}, \tag{3}$$

where L is the absolute radiance value [mW/(m^2 nm sr)] known from the integrating sphere lamp. K is different for each pixel, and therefore also corrects for any inter-pixel variations, also known as Photo Response Nonuniformity (PRNU) [10]. The K matrix is visualized in Figure 3. The brighter areas, such as for wavelengths close to 400 nm and above 700 nm, indicate that a larger value is needed to convert from counts to radiance. This can lead to higher radiometric uncertainties after calibration for the brighter areas.

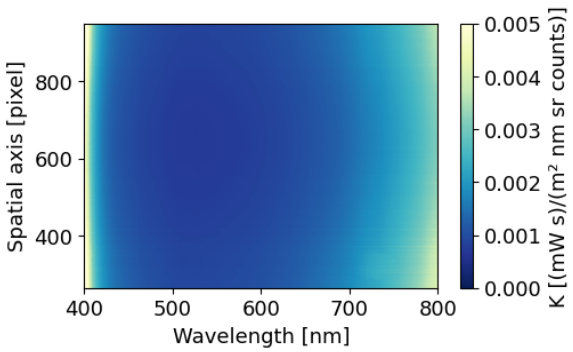

Figure 3: Radiometric calibration coefficients.

The uncertainty of the radiometric calibration coefficients was estimated by radiometrically calibrating a single frame, subtracting it from a reference frame, and dividing the difference by the reference values to obtain the percentage difference. The uncertainties for the center line in the spectrogram, and the mean radiometric uncertainty (calculated as the mean of the columns, as the target was uniform), are shown in Figure 4. The center line shows that noise fluctuations increase uncertainty for all wavelengths. The mean radiometric uncertainty shows higher uncertainty for wavelengths below 450 nm and lowest uncertainty of around 0.5% between 500 nm and 600 nm.

To estimate the full radiometric uncertainty of the final data, other factors should be included, such as linearity of the sensor response (both with increasing light intensity and exposure time), polarization sensitivity and uncertainties of the calibration source.

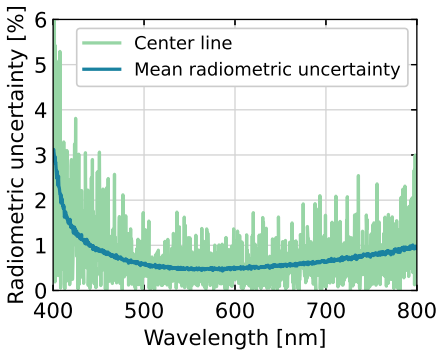

Figure 4: Radiometric uncertainty of calibration coefficients.

4. Sensor Characteristics

Data from radiometric calibration (including dark images) and a set of images of the integrating sphere captured at different exposure times were used to investigate the sensor characteristics.

The pre-selected AOI was used during the analysis, focusing on pixels 428 to 1508 in the x-axis (spectral direction) and pixels 266 to 950 in the y-axis (slit height direction). The full sensor was characterized, but the results are shown for the pre-selected AOI only, as this is the relevant area for the HYPSO-1 mission. Average numbers are given as the mean $\pm$ Standard Deviation (SD).

Sensor noise characterization

The background signal in the sensor was estimated by using the dataset of dark images. A single dark frame, Figure 5, shows that the distribution of background signal is mostly uniform across the sensor and has no significant discrepancies. The average value overall was found to be 8.01 ± 0.8 counts out of a total of 4095 counts in a 12-bit image.

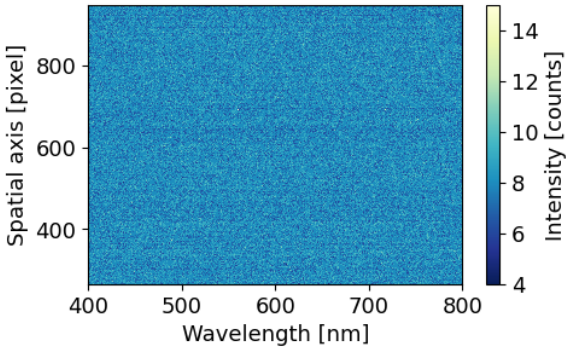

Figure 5: Single dark frame.

An average dark frame was calculated from the set of images, with an average value of 8.02 ± 0.27 counts. This confirms that averaging the set of images reduces the noise fluctuations, and that the average background value in the frames is about 8 counts.

The same calculations were repeated for datasets of different exposure times. The increase in the average background value was found to be less than 0.2 counts from exposure times 5 ms to 500 ms. The increase in noise fluctuations with exposure time was also found to be negligible.

Radiometric response

The data from radiometric calibration was also used to investigate the radiometric response. An example of a radiometric calibration frame is shown in Figure 6. A vignetting effect is visible, making the center of the image brighter (meaning a stronger signal) and the edges darker. No strong dust stripes or other optical deficiencies are immediately visible in the image.

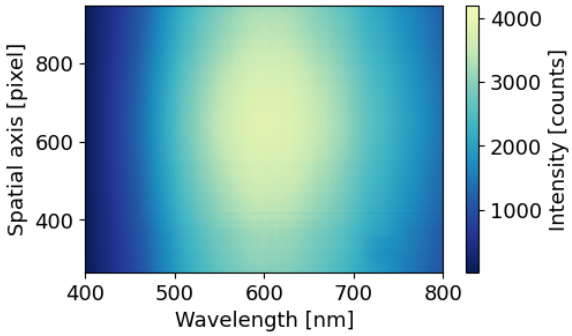

Figure 6: Radiometric calibration frame.

The absolute radiometric response was calculated as the average pixel response for each wavelength by taking the mean of the columns in the radiometric image. The smile effect was ignored as the absolute radiometric response was only used for visual inspection. The resulting absolute radiometric response is shown in Figure 7, together with the reference signal from the integrating sphere lamp, and the sensor and grating QEs. The absolute radiometric response near 400 nm is very weak, which is mostly due to low light level from the integrating sphere lamp at shorter wavelengths. The decrease in absolute radiometric response above 600 nm is mainly due to decreasing QE in the sensor and grating.

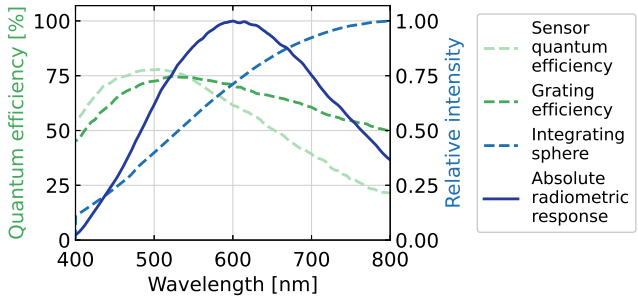

Figure 7: Absolute radiometric response, reference radiance from the integrating sphere tungsten halogen lamp and the QE of the sensor and the grating.

The relative radiometric response was calculated as the radiometric response divided by the absolute radiometric response, as described in Lenhard et al. [11], and is shown in Figure 8. This can be used to investigate the relative sensitivity of each spectral channel. The relative response shows a smudge (marked in the figure) at approximately 710 to 750 nm for pixels 300 to 400 on the spatial axis. The smudge causes a decrease in recorded signal, and might also cause other distortions as the signal is smeared out. The signal decrease is compensated for by the radiometric calibration. It is worth noting its presence, however, as that area will have lower radiometric accuracy from the lower signal level, and possible unwanted effects from the smear. The brighter area in the

center of the spatial axis comes from the vignetting effect, while the narrow horizontal stripes can indicate small dust particles on the slit.

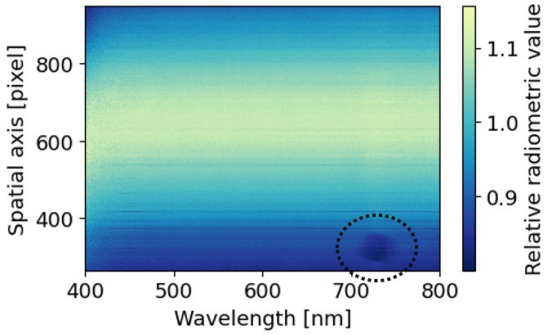

Figure 8: Relative radiometric response (radiometric response divided by absolute response). Marked area shows smudge.

Photon noise

The photon noise was investigated using the center line in the set of images from radiometric calibration. The measured noise, shown in Figure 9, was estimated as the SD of each pixel in the line, and sorted according to signal strength (varying for different wavelengths).

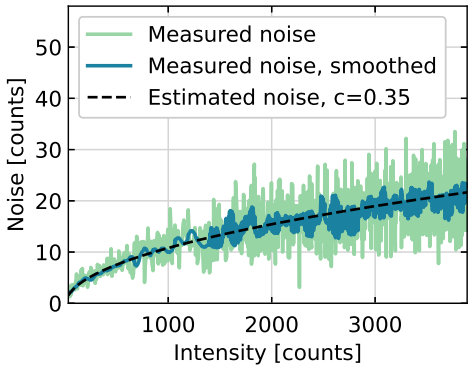

Figure 9: Photon noise, measured and estimated.

The theoretical photon noise was also calculated as the square root of the signal, S, and scaled with a proportionality constant c, following the relation

$$n_{\text{photon}} = c\sqrt{S}. \tag{4}$$

Choosing $c = 0.35$ gave the estimated noise to follow the measured noise, as shown in Figure 9. The measured noise was also smoothed (using a Bartlett window function) to make an easier comparison with the estimated noise.

Linearity of sensor response

The linearity of the sensor response with exposure time was examined using the set of images of the integrating sphere captured at different exposure times. A pixel that was nearly saturated in the highest exposed image was found. The value of this pixel was plotted for each exposure time, as seen in Figure 10. It can be seen that measured points follows the linear fit, meaning that the assumption of a linear sensor response with exposure time holds.

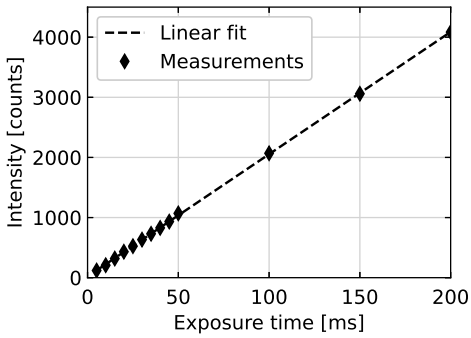

Figure 10: Linearity of sensor response with exposure time.

A nonlinear behavior is expected for low exposure times (less than 10 ms), where readout noise and dark noise fluctuations are expected to dominate. To explore this behavior, however, more measurements in this region are needed. For higher exposure times (more than 10 ms) the sensor response is expected to behave linearly, which is confirmed by the measurements.

5. Full Width at Half Maximum

The FWHM was calculated using the mercury and argon spectral calibration data. The peaks were identified, and the width at half maximum of each was found for several positions along the spatial axis. These include the mercury emission lines 435.85 nm and 546.07 nm, and the argon lines 696.54 nm, 706.72 nm, 738.40 nm, and 763.51 nm (other detected peaks known to be double peaks were excluded).

The resulting FWHM values are shown in Figure 11. It can be seen that they vary between 3.5 and 4.5 nm in the desired spectral range. The average FWHM for the selected wavelengths along the spatial axis (different slit height positions) was calculated to be 3.93 ± 0.30 nm.

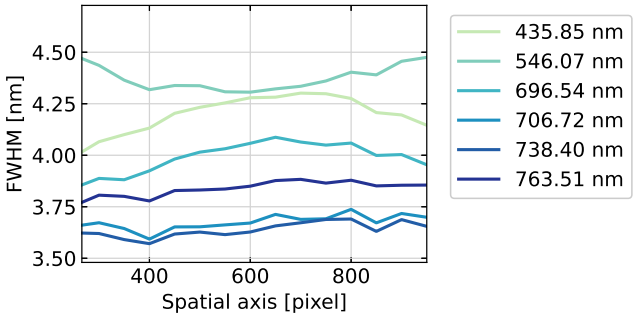

Figure 11: FWHM for argon and mercury spectral lines as a function of slit height.

Figure 11 also shows that it is the shorter wavelengths that have the broadest peaks, while the peaks close to 700 nm are narrowest. This suggests that the optimal focus was set in favor of the longer wavelengths. Most wavelengths follow a trend where the FWHM is lower at the edges of the spectrogram (low and high spatial pixels), while the line at 546.07 shows the opposite behavior. All values are below 4.5 nm, which is within the set requirement of 5 nm spectral resolution for the HYPSO-1 mission.

6. SMILE AND KEYSTONE

Smile is the change of central wavelength as a function of field position, while keystone is change in magnification as a function of wavelength. Together, they create a warping effect on the recorded image. This can be measured by creating a set of control points on a grid recorded by the HSI. The points can then be mapped to a straight reference grid to unwarp the image. The map that is created can be further used to correct for smile and keystone in other images [12].

For the smile and keystone characterization, a Zeiss Makro-Planar 100 mm f/2 objective was used as a collimating unit in combination with a striped pattern to provide points in focus in the spectrogram at a close distance to the target. The full setup and method is described in Henriksen et al. [13], based on the method presented in Lawrence et al. [12]. Ground Control Points (GCPs), the points measured, were created in the spectrogram using the argon and mercury spectral lamps, in combination with the striped pattern and the camera objective collimating the light. The location of the points were detected and used to make a two-dimensional quadratic polynomial distortion model. The model coefficients were then used to correct the spectrograms by mapping the pixels to the correct position and estimating new values with interpolation for non-integer pixel positions.

The pixel shift caused by smile before and after correction is shown in Figure 12. The curve before correction is not symmetric, which is due to spectral tilt as the slit was not aligned perfectly straight during assembly. Both smile and spectral tilt are reduced by the correction. The amount of smile was calculated as the difference between the minimum and maximum pixel positions for each of the spectral lines, and the average value was found to be 3.58 pixels before correction and 0.38 pixels after correction. The maximum smile was found to be 4.05 pixels and 1.05 pixels before and after correction, respectively.

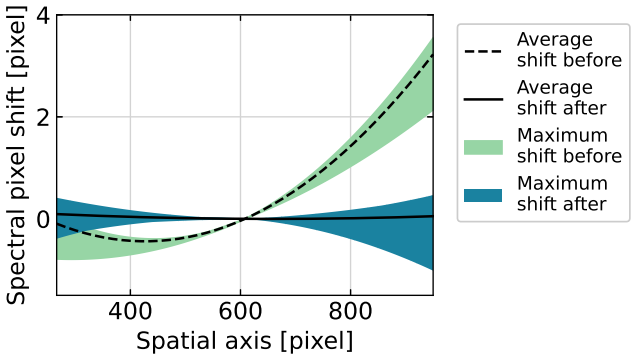

Figure 12: Pixel shift due to smile before and after correction. The maximum values (green and blue) shows the most extreme smile effects detected.

The maximum pixel shift due to keystone is shown in Figure 13. The keystone effect is less apparent than smile, but is also reduced by the correction. The amount of keystone was calculated as the maximum shift of the horizontal lines in the image. It was found to be 1.72 pixels before correction and 0.56 pixels after correction.

The requirements for both smile and keystone after correction are less than 1 pixel shifted due to the distortion. The average smile effect after correction of 0.38 pixels is within the required value, while the maximum smile of 1.05 pixels is just above the requirement. Keystone is within the requirement with the maximum value of 0.56 pixels shifted after the correction.

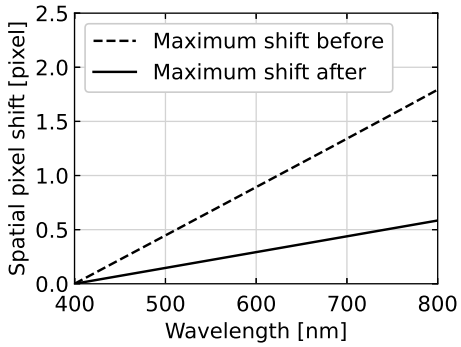

Figure 13: Maximum pixel shift detected due to keystone before and after correction.

Figure 14 shows the characterization data used before and after correction, which illustrates the effect of the correction. The full spatial axis, exceeding the AOI, is used and the spectral axis is cropped to focus on a smaller set of wavelengths to better visualize the effect. Smile in the data before correction can be seen as the curved lines, while keystone is not as apparent. After correction, the curved lines appear straight, indicating less smile in the data.

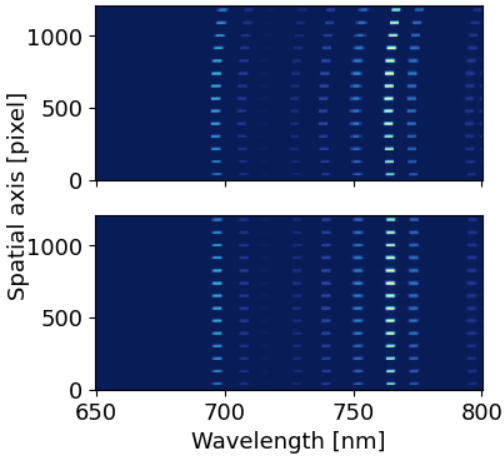

Figure 14: Cropped area of smile and keystone characterization data before (top) and after (bottom) correction. Note that the spatial axis is not cropped to AOI, showing a larger area than for intended use.

7. POLARIZATION SENSITIVITY

For polarization sensitivity analysis a linear glass polarizing filter (#46-574, Edmund Optics) was used. Polarization sensitivity was measured using the EM to limit unnecessary wear on the FM. The polarizing filter was mounted in front of the HSI observing the integrating sphere used for radiometric calibration. The filter was then rotated in steps of 15 degrees, in a range from 0 to 180 degrees. Sets of 10 spectrograms were acquired at each step, and averaged images from these sets used to estimate the final polarization sensitivity.

The measured signal, averaged for all pixels in the AOI varying with the polarizer angle is shown as crosses in Figure 15, together with a sinusoidal fit made to the data points. Some of the crosses deviate slightly from the sinusoidal shape, which is likely a result of the filter being rotated by hand.

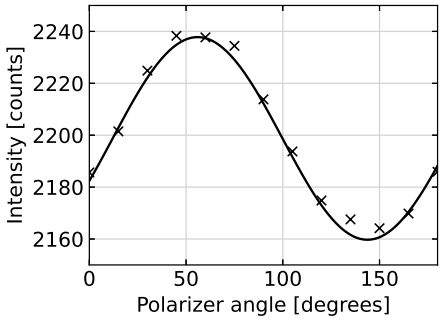

Figure 15: Sinusoidal fit (line) to averaged data points for each polarization angle (crosses).

The polarization sensitivity, $P_{\text{sensitivity}}$, was then calculated as

$$P_{\text{sensitivity}} = \frac{P_{\text{max}} - P_{\text{min}}}{P_{\text{max}} + P_{\text{min}}},$$

where P_{max} is the maximum value [counts] and P_{min} the minimum value [counts] in each pixel for all polarization angles, as defined in Mcclain et al. [14]. The calculated polarization sensitivity for each wavelength is plotted in Figure 16, and shows that all wavelengths over 410 nm have a polarization sensitivity below 5%.

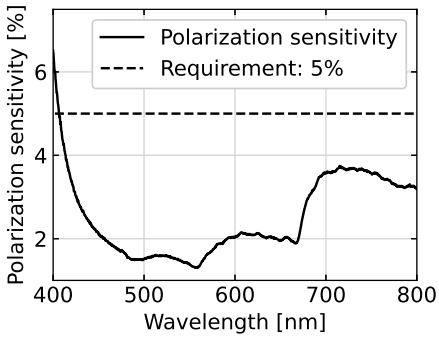

Figure 16: Calculated polarization sensitivity.

The uncertainty was estimated as the SD of the polarization sensitivity calculated with the different datasets. The calculation showed an uncertainty below the required 0.2% in the range of 500 nm to 700 nm, increasing to about 0.25% for wavelengths above 700 nm.

8. SPATIAL FOCUS TEST

A simple test was done to investigate the spatial focus at different wavelengths. A sharp transition from a bright to dark area was used as a target. This is commonly used for Earth Observation (EO) instruments to simulate transitions from bright clouds to dark ocean [15]. The target was created by 3D printing a black target cap that was illuminated by a uniform light source in front.

The 3D printed target was formed as a cylinder with the opening in one end half-closed, creating the sharp transition edge between the dark (closed) and bright (open) area. It was printed using an Original Prusa i3 MK3 with a resolution of 0.2 mm and black PolyLactic Acid (PLA) filament. It was covered with black matte tape inside after printing to reduce internal reflections. The Zeiss Makro-Planar 100 mm f/2 objective was used as a collimating unit with the 3D print fastened to one end. The length of the 3D print was made so that the sharp edge was in focus when attached to the collimating objective. The integrating sphere was used as the stable light source to minimize light fluctuations.

The resulting spectrogram is shown in Figure 17. The bright to dark transition can be seen at approximately spatial pixel 700. For the shorter and longer wavelengths at the edges of the spectrogram, the transition line becomes more blurry. This could be due to optical effects of the lenses since the sharpest response is expected to be in the center of the lens and more aberrations are expected at the edges. This should, however, be kept in mind when analyzing the final data and using the shorter and longer wavelengths as it will affect the spatial resolution per wavelength.

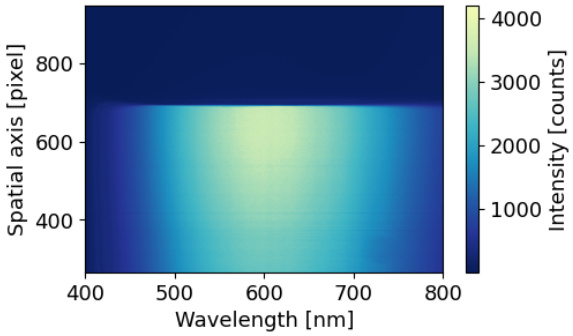

Figure 17: Captured frame of the black and white scene.

Figure 18 shows a cropped view of the transition line for a set of wavelengths to better investigate how the steepness of the bright to dark transition varies with wavelength. The sharpest edge was found at 600 nm, which is the designed center wavelength, closely followed by the lines at 550 nm and 650 nm. For the shorter and longer wavelengths, such as 450 nm and 750 nm, however, the transition is more gradual and covers more than 10 pixels from the bright to the dark transition. This suggests that a sharp edge in the image is smeared out and results in poorer spatial resolution for the wavelengths considered. Simulations done with ray tracing software (Zemax) show the same trends. The smallest spot size is at 600 nm and larger spot sizes at 400 nm and 800 nm.

In Figure 18 a small bump can also be seen for some of the wavelengths at approximately spatial pixel 710 nm. This could be caused by irregularities in the 3D printed part. A higher quality black and white scene is suggested to investigate this further. It is also worth noting that the Zeiss objective used as the collimating unit could also contribute to aberrations since the objective itself is not perfect. The test confirms that the design is optimized for 600 nm, and that more aberrations are expected at shorter and longer wavelengths than the center wavelength.

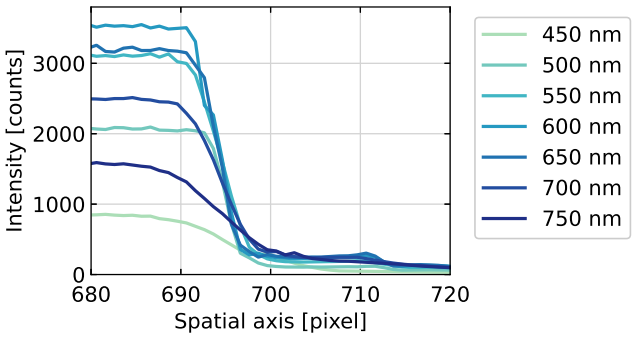

Figure 18: Lines showing defocus at shorter and longer wavelengths in the area close to the edge on the spatial axis.

9. Conclusions and Further Work

The HYPSO-1 hyperspectral imaging payload was calibrated and characterized prior to launch. The spectral and radiometric calibration coefficients and uncertainties have been determined. The full spectral range available at the sensor was found to be 224 to 962 nm, and the desired spectral range of 400 to 800 nm was shown to be within the chosen AOI. The FWHM was found to be between 3.5 to 4.5 nm for all wavelengths, which lets spectrally binning 9 pixels to increase SNR without losing spectral resolution be achievable [3]. Sensor characteristics, such as background signal and noise in dark images, photon noise and linearity of the sensor response, were identified and the values found were as expected. A summary of the selected HSI requirements and the corresponding measured values is shown in Table 5, and shows that most values are within the requirements.

Table 5: **Comparison of the selected HSI requirements and the measured values.**

Parameter	Requirement	Measured value
Sensor response	Linear	Linear
FWHM	< 5 nm	Between 3.5 nm and 4.5 nm (3.93 nm on average)
Smile after correction	< 1 pixel	0.38 pixels (average), 1.05 pixels (maximum)
Keystone after correction	< 1 pixel	0.56 pixels
Polarization sensitivity	$< 5\%$	$< 5\%$ above 410 nm
Uncertainty of polarization sensitivity	$< 0.2\%$	$< 0.2\%$ in the range 500 to 700 nm

For future HYPSO missions, a thorough characterization with varying temperature should take place. Preliminary work has been done in Prentice et al. [16], but more detailed characterizations should be performed. Both background signal, noise fluctuations, and radiometric and spectral characterizations should be measured as a function of temperature. Further, setups to investigate stray light should be developed, and more detailed characterization of the optical response should be done by measuring the PSF for multiple locations in the spectrogram.

After launch the HYPSO-1 HSI should be calibrated in-orbit, both spectrally and radiometrically. In-orbit spectral calibration is needed to ensure no spectral shifts occurred during launch, and no shifts happen during commissioning. In-orbit radiometric calibration should be done to continuously update the calibration coefficients in case of degradation in the sensor or browning of the lenses due to radiation. As the HYPSO-1 satellite has no calibration equipment on-board, vicarious calibration techniques must be developed and used.

Acknowledgments

This work was supported by the Research Council of Norway through the Centre of Excellence funding scheme (NTNU-AMOS, grant no. 223254) and the IKTPLUSS project MASSIVE (grant no. 270959), the Norwegian Space Agency, and the European Space Agency through PRODEX (no. 4000132515). The authors would like to thank Evelyn Honoré-Livermore, Mariusz E. Grøtte and the rest of the HYPSO-team for good discussions, debugging software and general support, Volker Kirschner and Simon Strotmann for interesting conversations and help with Zemax simulations, and Lise Lyngsnes Randeberg for access to the optical calibration lab at NTNU.

References

[1] A. Zuccaro Marchi, L. Maresi, and M. Taccola, "Technologies and designs for small optical missions," in *Proc. SPIE 11880, International Conference on Space Optics – ICSO 2018, 111801Z*, 2019.

[2] F. Sigernes, M. Syrjäsuo, R. Storvold, J. Fortuna, M. E. Grøtte, and T. A. Johansen, "Do It Yourself Hyperspectral Imager for Handheld to Airborne Operations," *Optics Express*, vol. 26, no. 5, 2018.

[3] M. E. Grøtte, R. Birkeland, E. Honoré-Livermore, S. Bakken, J. L. Garrett, E. F. Prentice, F. Sigernes, M. Orlandic, J. T. Gravdahl, and T. A. Johansen, "Ocean Color Hyperspectral Remote Sensing with High Resolution and Low Latency – the HYPSO-1 CubeSat Mission," *IEEE Transactions on Geoscience and Remote Sensing*, 2021.

[4] E. F. Prentice, M. E. Grøtte, F. Sigernes, and T. A. Johansen, "Design of a hyperspectral imager using COTS optics for small satellite applications," in *Proc. SPIE 11852, International Conference on Space Optics – ICSO 2020, 1185258*, 2021.

[5] T. Skauli, "Feasibility of a Standard for Full Specification of Spectral Imager Performance," *Proc. of SPIE: Hyperspectral Imaging Sensors: Innovative Applications and Sensor Standards*, vol. 10213, pp. 1–12, 2017.

[6] J. Bowles, M. Kappus, J. Antoniades, M. Baumback, M. Czarnaski, C. O. Davis, and J. Grossmann, "Calibration of inexpensive pushbroom imaging spectrometers," *Metrologia*, vol. 35, no. 4, pp. 657–661, 1998.

[7] M. B. Henriksen, E. F. Prentice, C. M. van Hazendonk, F. Sigernes, and T. A. Johansen, "A do-it-yourself VIS/NIR pushbroom hyperspectral imager with C-mount optics," [manuscript in preparation].

[8] R. R. Li, R. Lucke, D. Korwan, and B. C. Gao, "A Technique For Removing Second-Order Light Effects From Hyperspectral Imaging Data," *IEEE Transactions on Geoscience and Remote Sensing*, vol. 50, no. 3, pp. 824–830, 2012.

[9] R. Gordon, "Atmospheric correction of ocean color imagery in the Earth Observing System era," *Journal of Geophysical Research*, vol. 102, no. D14, pp. 17 081–17 106, 1997.

[10] F. Ewald, T. Kölling, A. Baumgartner, T. Zinner, and B. Mayer, "Design and characterization of specMACS, a multipurpose hyperspectral cloud and sky imager," *Atmospheric Measurement Techniques*, vol. 9, no. 5, pp. 2015–2042, 2016.

[11] K. Lenhard, A. Baumgartner, and T. Schwarzmaier, "Independent laboratory characterization of NEO HySpex imaging spectrometers VNIR-1600 and SWIR-320m-e," *IEEE Transactions on Geoscience and Remote Sensing*, vol. 53, no. 4, pp. 1828–1841, 2015.

[12] K. C. Lawrence, B. Park, W. R. Windham, and C. Mao, "Calibration of a Pushbroom Hyperspectral Imaging System for Agricultural Inspection," *Transaction of the ASAE*, vol. 46, no. 2, pp. 513–521, 2003.

[13] M. B. Henriksen, J. L. Garrett, E. F. Prentice, A. Stahl, and T. A. Johansen, "Real-time corrections for a low-cost hyperspectral instrument," in *10th Workshop on Hyperspectral Image and Signal Processing, Evolution in Remote Sensing (WHISPERS)*, 2019.

[14] C. R. Mcclain and G. Meister, "Mission Requirements for Future Ocean-Colour Sensors," IOCCG, Dartmouth, Canada, Tech. Rep., 2012.

[15] P. Coppo, A. Taiti, L. Pettinato, M. Francois, M. Taccola, and M. Drusch, "Fluorescence imaging spectrometer (FLORIS) for ESA FLEX mission," *Remote Sensing*, vol. 9, no. 649, 2017.

[16] E. F. Prentice, M. B. Henriksen, T. A. Johansen, F. N. Medina, and A. G. S. Juan, "Characterizing Spectral Response in Thermal Environments, the HYPSO-1 Hyperspectral Imager," in *Proc. IEEE Aerospace*, 2021, [accepted].

BIOGRAPHY

Marie Bøe Henriksen *received her M.Sc. degree in Engineering Cybernetics at the Norwegian University of Science and Technology (NTNU) in 2019, and is currently pursuing her PhD related to hyperspectral imaging in drones and small satellites with the same department. She is focusing on calibration and characterization activities with small and low-cost hyperspectral imagers. Her research interests include laboratory calibration methods, optical characterization setups, stray light and second order light correction, and smile and keystone correction.*

Elizabeth Frances Prentice *is a PhD researcher in the Department of Engineering Cybernetics at the Norwegian University of Science and Technology (NTNU). She is researching optical remote sensing and mechanical integration for small satellites and robotic agents. She has been responsible for hardware development and assembly / integration / testing (AIT) on the HYPSO-1 CubeSat mission at NTNU. She earned a MSc in Applied Earth Science from TU Delft (Delft, the Netherlands, 2016), a BSE in Aerospace Engineering from the University of Michigan (Ann Arbor, MI USA, 2011), and has several years experience in dimensional engineering at a design-for-manufacturing consultancy firm.*

Tor Arne Johansen *received the MSc degree in 1989 and the PhD degree in 1994, both in electrical and computer engineering, from the NTNU, Trondheim, Norway. From 1995 to 1997, he worked at SINTEF as a researcher before he was appointed Associated Professor at the NTNU in Trondheim in 1997 and Professor in 2001. He has published several hundred articles in the areas of control, estimation and optimization with applications in the marine, aerospace, automotive, biomedical and process industries. In 2002 Johansen co-founded the company Marine Cybernetics AS where he was Vice President until 2008. Prof. Johansen received the 2006 Arch T. Colwell Merit Award of the SAE, and is currently a principal researcher within the Center of Excellence on Autonomous Marine Operations and Systems (NTNU-AMOS) and director of the Unmanned Aerial Vehicle Laboratory at NTNU and the SmallSat Laboratory at NTNU. He recently co-founded the spin-off companies Scout Drone Inspection, UBIQ Aerospace and Zeabuz.*

Fred Sigernes *is a full Professor in optics and atmospheric research at the University Centre in Svalbard (UNIS), and he is head of the Kjell Henriksen Observatory (KHO) at Breinosa. He is a team leader for the ground-based activity at the Birkeland Centre for Space Science (BCSS) at University of Bergen (UiB) and Professor II at the Center of Excellence on Autonomous Marine Operations and Systems (AMOS) at the Norwegian University of Science and Technology (NTNU). His main expertise is spectroscopy with focus on aurora.*